Testing and modelling of stiffened aluminium panels subjected to quasi-static and low-velocity impact loading

D. Morin[a,b,*], B. L. Kaarstad[b,1], B. Skajaa[b,2], O. S. Hopperstad[a,b], M. Langseth[a,b]

[a] *Centre for Advanced Structural Analysis (CASA), NTNU, Norwegian University of Science and Technology (NTNU), NO-7491, Trondheim, Norway*
[b] *Structural Impact Laboratory (SIMLab), Department of Structural Engineering, NTNU, NO-7491 Trondheim, Norway*

Abstract

The behaviour and failure of stiffened panels made of the aluminium alloy AA6082-T6 is investigated under quasi-static and low-velocity impact loading conditions. The strain rate and inertia effects are found to be negligible suggesting that quasi-static tests might be representative for low-velocity impacts where a large mass is placed on the impactor. A simplified approach to the finite element modelling of aluminium panels under impact loading, including a regularised failure criterion, is proposed and validated against the experimental data. The effect of mesh size is investigated with shell elements of various sizes in the range from 1 to 5 times the thickness. A good correlation is obtained between experiments and simulations for fine meshes, while large shell elements have difficulties to initiate and propagate properly the observed cracks.

Keywords: Aluminium alloys, Impact loading, Design, Finite element analysis

---

*Corresponding author
[1] Currently at Norconsult, Oslo, Norway
[2] Currently at Betonmast Selvaagbygg AS, Oslo, Norway

1. Introduction

Aluminium alloys are important in design of lightweight structures due to their good strength-to-weight ratios. This advantage combined with flexible and cost-efficient extrusion processes have enabled the application of aluminium alloys in several business sectors, including the automotive industry [1] and the oil and gas industry. In the latter, multi-stiffened aluminium panels are used in a wide range of applications from walls and floors in offshore containers to hulls and decks in high speed ferries [2].

As stiffened aluminium panels are often basic building blocks of offshore structures, the research community has addressed the buckling resistance of these components over the past 15 years, e.g. Aalberg et al. [3] and more recently Paulo et al. [4]. At the same time, steel structures have been thoroughly investigated in the literature, with studies including laboratory scaled experiments [5] to full-scale testing [6], analytical developments [7], and modelling and simulation with non-linear finite element techniques [8]. In the latter class of studies, the emphasis has often been on finite element modelling with shell elements of various sizes, as offshore structures are usually rather large and thus prevent the use of fine meshes [9]. A thorough literature review of this particular topic has been recently published by Calle and Alves [10], where the different approaches proposed in the literature for modelling of offshore steel structures subjected to impact scenarios are presented.

Compared to steel structures, modelling of aluminium structures may raise new challenges due to their anisotropic properties [11]. Moreover, structures are usually built from several extruded parts that are welded together. Welding techniques for aluminium structures such as metal inert gas (MIG) welding and friction-stir welding (FSW) introduce heat-affected zones (HAZ) which exhibit lower strength than the base material to be joined [12, 13]. These particular features make the simulation of impact loading on aluminium structures using non-linear finite element methods challenging with regards to constitutive modelling.

Over the past decades, the numerical modelling of aluminium alloys has significantly improved with the development of advanced yield functions. An example is the yield function proposed by Barlat et al. [14] which is able to describe the complex anisotropic yielding and plastic flow of most of the aluminium alloys in plane stress states. A drawback of these advanced models is the cost linked to the identification of parameters. Calibration of these yield functions requires at least several tensile tests in different directions with respect to the extrusion or rolling direction, as many parameters are involved in their mathematical formulations. Even if great progress has been made in terms of calibration of these models using for instance crystal-plasticity methods [15, 16, 17], the industrial use of such approaches is still challenging and simplified methods are required.

Under impact loading, failure is most likely to occur and has to be accounted for in the design of an aluminium structure. Recent works [18, 19] have highlighted that ductile failure in aluminium alloys is strongly dependent on the stress state. Moreover, failure in aluminium alloys can also be strongly anisotropic, as illustrated for the AA 7075-T651 alloy by Fourmeau et al. [11]. As for the description of complex yielding and plastic flow, several models have been proposed to predict the observed stress state dependent failure of metals [18, 19, 20]. While accurate predictions in terms of fracture initiation can be obtained with these models, their calibration requires several material tests under different stress states, thus limiting their applications in an industrial context. Moreover, the full capacity of such fracture models relies on an accurate description of the local plastic flow and strain localization using refined solid element meshes. Therefore, it is not clear that these models would provide significant improvements in the ductile failure prediction when applied in simulations with large shell elements.

This study evaluates the response of stiffened aluminium panels subjected to impact loading. The panels are subjected to quasi-static and low-velocity impact loading using a cylindrical impactor oriented either longitudinally (in parallel) or transversally to the stiffeners. Based on the obtained experimental data, a constitutive model and a failure criterion suitable for numerical simulation of large-scale offshore structures are identified and evaluated using finite element models with different mesh sizes.

2. Material tests

The stiffened aluminium panels are composed of extruded profiles of alloy AA6082 in temper T6. The nominal chemical composition of the alloy is given in Table 1. AA6082 is the most common structural aluminium alloy due its combination of high strength, corrosion resistance and availability as rolled plates and extruded profiles of various form. Moreover, its mechanical properties are comparable in terms of yield strength to regular offshore steels. The aluminium panels are assembled by use of friction-stir welding and each panel consists of five extruded profiles, as shown in Figure 1. The extruded profile has two stiffeners with a thickness of 3 mm, while the base plate has a thickness of 4 mm. A small increase in thickness is found at both ends of the profile, delimited by a lip (see Figure 1). The material properties of the base plate and the stiffeners are obtained from tensile testing using the specimen shown in Figure 2a. The plastic anisotropy of the extruded profile is investigated by performing tensile tests in three directions with respect to the extrusion direction. These tests are done for the base plate only. The macroscopic properties of the heat-affected zone (HAZ) are evaluated using the slightly bigger specimen depicted in Figure 2b. These tests will be referred as cross-weld tensile tests.

Digital Image Correlation (DIC), using a in-house software [21], and a grip extensometer are applied to measure strains. The gauge length of the extensometer is 35 mm in the tests of the base plate and stiffener material and 57.5 mm in the tests of the heat-affected zone around the welds, respectively. The force is measured by the load cell of the universal testing machines used to perform the tensile tests.

	Si	Fe	Cu	Mn	Mg	Cr	Zn	Ti	Others
Min (%)	0.70			0.40	0.60				0.05
Max (%)	1.30	0.50	0.10	1.00	1.20	0.25	0.20	0.10	0.15

Table 1: Nominal chemical composition of the AA6082 in temper T6.

The tensile tests were carried out at a speed of 1.35 mm/min for the base plate and stiffener materials and 2.1 mm/min for the HAZ to ensure a quasi-static strain rate. The engineering stress-strain curves are shown in Figure 3a for the base plate material and exhibit relatively strong anisotropy of the yield stress. The plastic strain ratios (or Lankford coefficients) are presented in Table 2 and it is evident that also the plastic flow is anisotropic. From Figure 3b, it can be seen that the stiffener material exhibits a somewhat lower yield stress, while the overall shape of the engineering stress-strain curve is similar to that of the base plate material. It is believed that a difference in cooling rate could be responsible for the lower yield stress as this process parameter can have a large impact on the mechanical properties of a 6xxx alloys.

The engineering stress-strain curve from the HAZ is shown in Figure 3b. The yield stress is reduced and the work-hardening increased compared with the base plate and stiffener materials. These results are in accordance with existing experimental data for AA6082 in temper T6 [12]. It should be noted that material behaviour within the HAZ is strongly heterogeneous and thus the engineering stress-strain curve in Figure 3b represents the overall behaviour of the HAZ. Figure 4 shows the strain field determined by DIC on a cross-weld tensile test and demonstrates the strongly heterogeneous strain field even at low strain levels.

R_0	R_{45}	R_{90}	R_0 (stiffener)
0.41	1.53	0.98	0.47

Table 2: Plastic strain ratios of AA6082 in temper T6.

3. Component tests

3.1. Test set-up and procedures

The component tests are carried out under both quasi-static and low-velocity impact loading. The impactor is shown in Figure 5a. It has a cylindrical shape with hemispherical end caps to avoid crack initiation at sharp edges. Two loading configurations are investigated. The impactor is placed either transversally to or longitudinally (in parallel) with the stiffeners, later referred to as transverse or longitudinal orientation of the impactor. The plates are fixed in-between two massive steel frames made of welded square hollow sections (thickness 20 mm, 100 mm width) (Figure 5b). In the bottom frame, 50 mm wide cut-outs make possible the use of continuous stiffeners in the aluminium panel. To increase the support of the plates, 8 mm thick L profiles are positioned between the plate and the bottom frame, reducing the gap of 50 mm to 10 mm in the area of the cut-outs. Teflon sheets are placed at the interfaces between the panel and the top and bottom frames to reduce the effect of friction forces (Figure 5 c). A total of eight M16 bolts in property class 12.9 (i.e., two bolts per side) are used to keep the plate in position between the top and bottom frames during testing. The bolts are only loosely tightened. The specially designed rig is then fixed to a rigid foundation. A lubricant is applied on the impactor to reduce the effect of friction. For more details on the clamping system, the reader is referred to Gruben et al. [22].

The quasi-static tests are carried out using a hydraulic jack to apply the load at a rate of 10 mm/min (Figure 6a). The force level is recorded by a 1000 kN load cell, while the relative displacement between the impactor and the bottom frame is measured by two laser extensometers. The two extensometers are targeting each side of an aluminium beam placed on top of the impactor (Figure 6a). The two laser extensometers placed on each side of the bottom frame are used to evaluate any misalignment of the test rig with respect to the impactor. The local deformations of the plate and stiffeners are monitored by a set of two cameras placed under the test rig.

The impact tests are carried out using a pendulum accelerator [23]. The impactor is installed on a trolley with a total mass of 1431 kg (Figure 6b). The tests are carried out at impact velocities in-between 2 and 3 m/s. The impact velocity of the trolley is measured using a set of photocells placed in front of the stiffened plate. The clamping system previously described is fixed to the reaction wall in a vertical position (Figure 6b). The velocity and displacement of the trolley during the impact are calculated based on the force-time curve measured in the load cell on the trolley. A set of high speed cameras is used to monitor the impact area at a frame rate of 15000 frames/s. Additionally, these cameras are used to measure the displacement of the impactor and control the measurements from the load-cell (Figure 6b). Due to limited space between the plate and the rigid wall, no cameras are monitoring the local deformation of the plates.

3.2. Results from quasi-static tests

The force-displacement curves from the quasi-static tests are shown in Figure 7a and b for the transverse and longitudinal impactor orientations, respectively. The two replicates in each configuration show little scatter in stiffness and maximum force. The replicates of the transverse and longitudinal impactor orientations are defined as $QSTE_1$, $QSTE_2$ and $QSLE_1$, $QSLE_2$, respectively.

When loading with the transverse orientation of the impactor, three types of fracture are observed (Figure 8a). First a crack is initiated and developed in the stiffeners (designated "1" in Figure 8a). The effect of this crack is visible on the force-displacement curve in Figure 7a at a displacement of about 60 mm for the first specimen ($QSTE_1$) and 65 mm for the second specimen ($QSTE_2$). After the first crack has propagated through the stiffener, the plate still carries the load with a reduced stiffness until a second crack is initiated on either one or both sides of the impactor (designated "2" in Figure 8a). Specimen $QSTE_1$ exhibits a non-symmetric crack propagation, i.e., the second crack, which is parallel to the stiffeners, is propagating on only one side of the impactor. The steep reduction in the force level for the $QSTE_2$ specimen after 80 mm of indentation is due to a third crack initiating perpendicularly to the second crack and propagating under the impactor (designated "3" in Figure 8a). A ductile failure mechanism appeared to be dominant in the stiffener (1) and in the plate (2), while the crack propagating below the impactor (3) seems to be the results of a through-thickness shear failure mechanism.

For the longitudinal orientation of the impactor, fracture is only observed in the plate (Figure 8b). The sudden loss of load-carrying capacity of the plate as show in Figure 7b around 68 and 72 mm of indentation for the first and second specimen, respectively, is linked to a large crack propagating under the impactor.

While through-thickness shear fracture seems to be the dominant failure mechanism, a closer inspection of the camera recordings of the plate shows a surface crack initiating perpendicularly to the impactor (Figure 7b). This crack initiates at about 43 mm of displacement and propagates quite slowly until the crack suddenly runs under the impactor.

In both configurations of the impactor, the weld lines are subjected to plastic deformations only and no signs of cracking are observed. It is believed that the small lips on each side of the weld might have acted as local stiffeners and prevented localization to occur in the HAZ.

3.3. Results from low-velocity impact tests

The force-displacement curves of the low-velocity impact tests are shown in Figure 9a and b for the transverse and longitudinal orientations of the impactor, respectively. The impact velocity was in turn 2.42 and 2.61 m/s in the two tests DTE_1 and DTE_2 with transverse orientation of the impactor. In the two tests DLE_1 and DLE_2 with longitudinal orientation of the impactor, the impact velocity was 3.48 and 3.06 m/s, respectively. The two replicates show consistent results in terms of maximum force and overall ductility, while there is some scatter in the stiffness.

Figure 10 shows the fracture modes occurring in the two loading cases. In the tests with the impactor in the transverse direction, tensile failures are observed in the stiffeners (indicated with a red line in Figure 10a). Small cracks are also observed on the sides of the impactor (also indicated with a red line in Figure 10a). Due to the low impact speed, the impact energy was too low to propagate these cracks. In contrast, the impact energy is higher in the tests with the impactor in the longitudinal direction and full loss of load-carrying capacity is obtained by a crack propagating below the impactor, as illustrated in Figure 10b.

3.4. Comparison of quasi-static and low-velocity impact tests

A comparison of the force-displacement curves of the quasi-static and dynamic tests is shown in Figure 11a and b for the transverse and longitudinal orientations of the impactor, respectively. No significant effects of strain rate and inertia are found. This result seems reasonable as the AA6082 alloy in temper T6 has been found to be almost rate insensitive [24] and the impacting mass is significantly larger than the mass of the panels. The fracture modes are also found to be similar (Figure 8 and 10). From this comparison, it seems that quasi-static tests might be good representatives for low-velocity, large-mass impactor tests on stiffened aluminium panels, provided the material exhibits low rate sensitivity.

4. Material modelling

4.1. Constitutive model

To enable industrial applications of the simulation modelling, an isotropic elastic-plastic model was adopted, even if the investigated alloy exhibits a rather strong plastic anisotropy, as shown in Figure 3a and Table 2. The experimental and computational costs of employing an anisotropic plasticity model are large and not always possible within an industrial context. The same constitutive model is applied to the plate and stiffener materials as well as the HAZ. To capture the typical shape of the yield surface of an aluminium alloy [25], the Hershey-Hosford yield function [26, 27] is employed.

The yield function is expressed as

$$f = \varphi(\boldsymbol{\sigma}) - (\sigma_0 + R) \leq 0 \tag{1}$$

where σ_0 is the initial yield stress and R the isotropic hardening variable. The Hershey-Hosford equivalent stress is defined by:

$$\varphi(\boldsymbol{\sigma}) = \left[\frac{1}{2}\left(|\sigma_1 - \sigma_2|^a + |\sigma_2 - \sigma_3|^a + |\sigma_3 - \sigma_1|^a\right)\right]^{\frac{1}{a}} \tag{2}$$

where σ_1, σ_2, σ_3 are the eigenvalues of the Cauchy stress tensor $\boldsymbol{\sigma}$ and a is a material parameter controlling the shape of the yield surface. For FCC materials such as aluminium alloys, it is customary to set a equal to 8 based on lower scale analyses. Figure 12 shows the resulting Hershey-Hosford yield surface under plane stress conditions with a equal to 8 compared with the von Mises and Tresca yield surfaces.

The work hardening of the aluminium alloy is described by an extended Voce rule in the form

$$R = \sum_{i=1}^{N_R} R_i = \sum_{i=1}^{N_R} Q_i \left(1 - e^{-\frac{\theta_i}{Q_i} p}\right) \tag{3}$$

where p is the equivalent plastic strain, θ_i and Q_i represent the initial work hardening modulus and the saturation stress of hardening term R_i, and N_R is the number of terms. Two terms are used to represent the work-hardening of the plate and stiffener materials, while only one term is used for the HAZ.

The associated flow rule is used in this work to describe the plastic flow. Owing to the limited rate sensitivity of this alloy [24] and the negligible differences in response between quasi-static and dynamic components tests (Figure 11), a rate-independent formulation of plasticity is used.

4.2. Failure model

The Cockcroft-Latham failure criterion [28] is used to model ductile failure of the aluminium alloy. The failure criterion is here formulated as a damage evolution rule

$$\dot{D} = \frac{\langle \sigma_1 \rangle}{W_C} \dot{p} \tag{4}$$

where D is the damage variable, σ_1 is the maximum principal stress, $\dot{p}$ is the equivalent plastic strain rate, W_C the Cockcroft-Latham parameter, and $\langle x \rangle = \max(0, x)$ is the Macauley bracket. Failure is assumed when the damage variable D has reached a critical value D_C. Since the damage variable is not affecting the elastic-plastic behaviour of the material, D_C can be set to unity without loss of generality.

The Cockcroft-Latham failure criterion has the benefit of having only one parameter and therefore reduces the calibration cost. This damage evolution rule accounts for the main features of ductile failure under plane stress conditions such as a decrease of ductility from uniaxial tension to plane strain tension followed by an increase towards equi-biaxial tension. Failure will not be predicted for uniaxial compression and lower stress triaxiality, while pure shear will produce a rather large ductility [20]. However, failure under low triaxiality is not considered to be important in the present study because thin-walled structures (as the aluminium stiffened panels investigated here) will typically accommodate compression and shear loading by buckling leading to a locally tensile-dominated problem.

4.3. Computational considerations

The constitutive model is implemented in ABAQUS [29] as a user-defined material model for 3D and plane stress states. In ABAQUS/Explicit, the cutting-plane algorithm [30] is adopted for temporal integration of the constitutive relations, while a semi-implicit algorithm [31] is used in ABAQUS/Implicit. To ensure an accurate stress update, a sub-stepping scheme is employed. The maximum magnitude of the incremental deviatoric strain tensor is set to 10% and 1% of the strain to yielding for explicit and implicit simulations, respectively. If the strain increment is larger, sub-stepping will reduce the strain increment to its maximum allowable value.

ABAQUS/Standard requires the consistent tangent operator in addition to the updated Cauchy stress tensor. The consistent tangent operator is obtained here by means of numerical derivation using a central difference scheme. By setting the exponent a of the Hershey-Hosford yield function equal to 2, comparison with the built-in J_2 flow theory of ABAQUS/Implicit is possible. Similar results were obtained in simulation of a tensile test with solid elements both with regards to local response and equilibrium iterations, indicating a good accuracy of the computed consistent tangent operator.

Failure and crack propagation is handled by element elimination in the explicit simulations. The stress tensor is set to zero in each integration point where the damage variable D is equal to unity. Since this operation is carried out within one time step, elastic stress waves are released into the remaining mesh, thus creating some noise in the calculated forces in the simulations of the component tests. In ABAQUS/Explicit an element is removed when all integration points have reached failure. As will be shown below, this might be problematic when propagating a crack within the finite element mesh.

4.4. Parameters identification

The proposed constitutive model requires the input of the initial yield stress σ_0 and the parameters (θ_1, Q_1) and (θ_2, Q_2) of the two hardening terms. The initial yield stress σ_0 and the parameters (θ_1, Q_1) of the first hardening term are identified directly from the uniaxial tensile tests in the extrusion direction (denoted $0°$ in Figure 3a and b), using the true stress-strain curve computed based on the extensometer measurements. Here, the first hardening term is defined as the first to reach its saturation stress Q_1. The parameters (θ_2, Q_2) of the second hardening term are initially identified using the experimental measurements, but are later refined using a numerical model.

Reverse engineering of the tensile test in the extrusion direction is performed with a solid element model of the specimen in ABAQUS/Standard. The parameters θ_2 and Q_2 are modified manually until a satisfactory agreement is found between the test and the numerical simulation in the post-necking regime. The numerical model of the tensile test is shown in Figure 13a. Due to the assumption of isotropy and the neck taking place perpendicularly to the loading axis of the specimen, only 1/8 of the geometry is modelled. Within the grip length of the extensometer solid elements with characteristic size of 0.4 and 0.3 mm are used for the plate and stiffener materials, respectively, while a coarser mesh is used outside this area. Reduced integration with improved hourglass control is employed in these simulations. The specimen is loaded using a rigid analytical surface to represent the pinned connection. A frictionless interface is defined between the specimen and the pin using a surface-to-surface contact algorithm.

The results in terms of engineering stress-strain curves are shown in Figure 13b. A rather good agreement is obtained until an engineering strains of 0.12. The tail of the engineering stress-strain curve is not captured properly by the finite element model, but the obtained set of parameters is considered to be sufficiently accurate. Since the material exhibits marked anisotropy with low plastic strain ratio in the extrusion direction, the simulations cannot be expected to describe the experimental curves until failure occurs.

Prediction of ductile failure with a finite element model is a mesh-size dependent problem. A simple way to handle mesh-dependent parameters is to use a computational-cell approach, i.e., the element type (e.g. solid vs. shell) and mesh size is fixed during identification and application of the failure model [32]. While some material tests can be modelled correctly with shell elements of various sizes, this is not the case for the uniaxial tensile tests carried out in this study. A flat tensile specimen exhibits usually diffuse necking followed by localised necking and subsequently failure. While the diffuse neck scales with the specimen width, the local neck scales with the thickness of the specimen, and thus a rather fine mesh is required to accurately capture local necking and failure. It follows that a shell element model with mesh size greater or equal to the the thickness of the specimen will generally not provide a reliable estimate of the failure parameters. Shell elements with a characteristic element length l_e below the specimen thickness could be used to simulate the uniaxial tensile tests, but this would require use of non-local regularization to prevent excessive thinning [12]. This approach of combining very small shell elements and non-local regularization is not always suitable for the simulation of large structures due to the increased computational time.

One convenient method to obtain an element-size dependent fracture parameter for use in large-scale shell simulations, is to use the field measurements obtained by digital image correlation (DIC) on the specimen surface in the necking region. As illustrated in Figure 14a, the elongation Δl of a vector of length l_e in the initial configuration is extracted from the DIC measurements and used to define the boundary conditions for a single shell element with edge length l_e. This approach is very similar to the one proposed by Hogström et al. [33]. The shell element is then loaded under uniaxial tension until the elongation at failure in the experimental test is reached. The corresponding Cockcroft-Latham parameter W_C is then found by integrating the damage evolution rule (eq. 4) with a temporary W_C equal to 1 and a critical damage D_C equal to a very large number. By repeating this operation for different element length l_e, it is possible to evaluate the mesh dependency of the failure parameter W_C, as shown in Figure 14b. To enable a direct comparison between the plate and stiffener materials which have different thicknesses it is chosen to represent the size of the shell elements by the ratio l_e/t_e, where l_e is characteristic element length and t_e is the initial thickness of the shell element. This definition will also allow for extrapolation of the obtained data to larger thicknesses. It should be mentioned that boundary conditions extracted from a vector perpendicular to the loading axis of the uniaxial tensile test specimen could have been used if the plastic anisotropy of AA6082-T6 was incorporated into the constitutive model. By restricting the boundary conditions to uniaxial tension, a conservative estimate of the failure parameter should be obtained. This is motivated by the fact that the local stress state of a tensile test is usually drifting from uniaxial tension before necking towards plane strain at failure. Since the failure strain is decreasing between these two stress states, the failure locus is then underestimated by the proposed methodology.

4.5. Heat Affected Zone modelling

The component tests did not show any sign of failure in the HAZ of the AA6082-T6 plates, and therefore a simplified modelling approach is applied in the simulations of the component tests. The width of the HAZ is set to 20 mm in both the simulations of the cross-weld tensile tests (Figure 15a) and the component tests and it is assigned a single set of material parameters, i.e., the spatial variation within the HAZ is homogenized. This approach accounts for a weaker zone in the component tests, while being simple enough to be useful in an engineering context. As shown in Figure 4, the heterogeneous strain field in the HAZ makes impossible a direct identification of the parameters of the constitutive model.

A reverse engineering approach is employed to determine the work-hardening parameters θ_1 and Q_1 by iteratively comparing the results from a shell element model of the cross-weld tensile test to the experimental results. The elastic constants and the exponent a of the Hershey-Hosford yield function are given the same values as for the plate and stiffener material. The yield stress σ_0 of the HAZ is fixed to 150 MPa according to the cross-weld tensile tests. ABAQUS/Explicit with time scaling was employed to find the remaining parameters. This type of numerical simulations is mesh sensitive even before reaching maximum force due to the heterogeneous distribution of the material properties along the gauge length of the specimen. Accordingly, the material parameters are adjusted for different l_e/t_e ratios. Only small variations (± 5% of the values of the hardening parameters θ_1 and Q_1) are necessary to get a similar description of the engineering stress-strain curve of the cross-weld tensile tests (Figure 15b) for a large range of l_e/t_e ratios.

As already stated, the proposed approach is valid as long as failure does not occur in the HAZ. If failure occurs within the HAZ, a better description of the spatial variation in the material properties across the HAZ should be employed to enable prediction of strain localization [12, 34].

5. Numerical analyses

5.1. Finite element model

The numerical model used to evaluate the proposed modelling approach is presented in Figure 16. Due to the symmetries in the geometry and boundary conditions, only 1/4 of the structure is modelled. The full test rig is represented as a deformable body (apart from the impactor) to capture properly the stiffness of the aluminium panel and to ensure a correct representation of the boundary conditions. The steel frame is discretized with shell elements of 10 mm characteristic length and modelled as an elastic-perfectly plastic material with Young's modulus, Poisson's ratio and yield stress equal to 210000 MPa, 0.3 and 355 MPa, respectively. The bolts used to fasten the top frame to the bottom frame are discretized with beam elements of 16 mm diameter and modelled as an elastic-perfectly plastic material with Young's modulus, Poisson's ratio and yield stress equal to 210000 MPa, 0.3 and 1080 MPa, respectively. The connection between the different steel cross-sections and between the bolts and the top and bottom frames is ensured through a tie-constraint formulation.

The stiffened aluminium plate and the homogenized HAZ are modelled using reduced integration shell elements of various length to thickness ratio ($l_e/t_e = 1, 2, 3, 4, 5$). Since the stiffeners and the plate are sharing some nodes, the l_e/t_e ratio of the stiffeners is slightly larger than that of the plate. Uniform meshing is applied for the stiffened plates, leading to around 40000 elements for an l_e/t_e ratio of 1 and around 7000 elements for an l_e/t_e ratio of 5.

The impactor is modelled using a rigid body definition with a mesh size of 4 mm. The test rig and the impactor have the same mesh size independently of the l_e/t_e ratio of the stiffened plate to allow a one-to-one comparison of the numerical results. The Teflon sheets and lubricant are not included in the numerical model and replaced by a surface-to-surface contact definition between the aluminium stiffened plate and the steel parts (both the impactor and steel frames) with a small friction coefficient of 0.05.

Since the quasi-static and dynamic components exhibit similar force levels and failure mechanisms, only the quasi-static tests are simulated numerically. ABAQUS/Explicit is used for this purpose with time scaling to reduce the computation time. The velocity of the impactor is gradually increased using a smooth function over 10% of the simulation time and then kept constant until the end of the simulation. The simulation time is chosen to obtain negligible inertia effects.

The material properties identified in Section 4.4 are summarised in Table 3. Only the parameters for the finest shell mesh are reported here. To handle the mesh dependence, several sets of material parameters are used in accordance with the targeted mesh size. For the plate and stiffener materials, only the fracture parameter W_C varies with the mesh size, while the hardening parameters θ_1 and Q_1 depend weakly on the mesh size for the HAZ material.

	E (MPa)	ν (-)	σ_0 (MPa)	a (-)	θ_1 (MPa)	Q_1 (MPa)	θ_2 (MPa)	Q_2 (MPa)	W_C (MPa)
Plate	66000	0.3	271.5	8	36591.2	17.8	1300.0	88.0	64.3
Stiffener	66000	0.3	238.7	8	63294.5	36.6	1440.0	90.0	64.2
HAZ	66000	0.3	150.0	8	3450.0	140.0	-	-	-

Table 3: Material parameters for $l_e/t_e = 1$.

5.2. Results

The force-displacement curves obtained for the transverse impactor orientation are shown in Figure 17a. By including the test rig as a deformable body in the numerical model, the overall response is rather well reproduced in the simulations. A general observation is that increasing the element size produces a slight increase of the overall stiffness. The effect of a crack developing in the stiffener (between 60 and 65 mm of displacement) is rather well captured for $l_e/t_e = 1$ (Figure 17a). The simulations with larger aspect ratios l_e/t_e exhibit only limited mesh dependence, indicating that the proposed mesh scaling method is working correctly. This is confirmed by the comparison between the numerical and experimental displacements at which the first crack in the flange of the stiffener appears (Figure 17b). In the simulation, failure is assumed to initiate in a shell element when the integration point at mid-section reaches $D = 1$. It should be noted that the flange of the stiffener experiences a stress state close to uniaxial tension but with a small stress gradient through the thickness. Regarding the crack propagating into the web of the stiffener, all simulations predict that one or two elements remain intact near the plate (Figure 17d), while in the experiments complete failure of the stiffener web is observed (Figure 8b).

The simulations predict the force increase after the failure has propagated into the stiffener web, while the force reduction in the last part of the tests (around 80 mm) is not captured, independent of the mesh size. This force reduction is caused by the crack propagating below the impactor in the tests (denoted ”3” in Figure 8a), which is not predicted in the simulations. This is most likely caused by a combination of several effects. Firstly, the failure in the plate (next to the impactor, denoted ”2” in Figure 8a) is not predicted properly in the simulations, as shown in Figure 17c. In this region of the plate, the shell element is subjected to biaxial tension on the back face and biaxial compression on the front face (i.e., the impactor side). According to the Cockcroft-Latham criterion, damage will not evolve until the maximum principal stress becomes positive. Secondly, as stated in section 4.3, ABAQUS/Explicit will delete an element only when all integration points through the thickness have reached failure. In view of Figure 17c, these two factors affect the prediction of failure initiation and propagation in the plate. Indeed, failure in the integration points on the tensile side of the plate is usually predicted before the actual crack initiates in the experiments, but the integration points next to the impactor do not reach failure for the given displacement. This prevents the elimination of the element and therefore the propagation of a crack below the impactor. Finally, the mesh discretisation is probably a key issue in the prediction of the crack on the edge of and below the impactor. The impactor used in this study has a radius of 25 mm, while the element length is ranging from 4 to 20 mm for l_e/t_e equal to 1 and 5, respectively. The mesh has then to describe the impactor with 6 to 1 element and is therefore not accurate enough.

Also for the transverse impactor orientation, the simulated global response is in good agreement with the experimental data (Figure 18a), but the force level is slightly overestimated for large displacements. The finest mesh used in this study ($l_e/t_e = 1$) predicts the complete loss of load-carrying capacity of the structure rather accurately, while the other meshes predict structural failure either too late or not at all. The high-frequency oscillations observed in the force-displacement curves are caused by elastic stress wave generated when through-thickness integration points fail and the stress tensor is abruptly set to zero. Figure 18b shows the displacement required to initiate a crack in the plate under the impactor. While the location of the predicted cracks correlates rather well with the one observed in the tests (Figure 8b), crack initiation is delayed for l_e/t_e equal to 2 and 3. In the simulations with l_e/t_e equal to 4 and 5, material failure is not predicted at all. As discussed above, requiring that all through-thickness integration points must reach failure before deleting an element, prevents crack initiation and thus the complete loss of capacity of the structure. Notwithstanding, the simulated crack pattern (Figure 18c) for the finest mesh(es) is rather close to the one observed in the tests (Figure 8b). In particular, the FE models with $1 \leq l_e/t_e \leq 3$ are able to predict the crack developing perpendicularly to the impactor.

5.3. Discussions

From the results presented in section 5.2 it appears that, despite the regularized failure parameters, failure initiation can only be predicted correctly when a fine shell mesh with element size being equal to the thickness is used. In the investigated aluminium panels, even if failure initiation is captured properly for the finest meshes, the propagation of the cracks is still difficult to predict accurately.

According to the numerical results presented in Figure 17 d and 18 c, the different mesh sizes applied for the aluminium panels are still able to predict the crack locations accurately. Taking into considerations the numerical costs summarized in Table 4 and 5 for the transverse and longitudinal impactor orientations additional conclusions can be drawn. The numerical cost behind the use of a fine shell element mesh ($l_e/t_e = 1$) is quite important in term of normalised CPU time. Here the CPU time is normalised by the one required to solve the finest mesh. This increase in computational cost is linked to the large number of elements combined with a smaller initial stable time step. It is also shown in Table 4 and 5 that the differences in the computational cost for the $l_e/t_e = 3$, 4 and 5 meshes are small due to a similar number of elements and that the initial stable time step is the same. The time step in these numerical models is actually dominated by an element located in the test rig. In design of aluminium stiffened structures against impact loading, a mesh size of 3 to 4 times the thickness could be used in preliminary simulations. In the area where the damage parameter is rather large (in the present analyses 0.5), the mesh should then be refined towards an element aspect ratio of one.

l_e/t_e	Number of elements	Normalised CPU time	Initial time step (s)
1	41918	1	4.437e-07
2	14345	0.134	9.415e-07
3	9105	0.046	1.209e-06
4	7403	0.031	1.209e-06
5	6683	0.025	1.209e-06

Table 4: Summary of numerical models data for the transversal impactor orientation.

l_e/t_e	Number of elements	Normalised CPU time	Initial time step (s)
1	41918	1	4.437e-07
2	14424	0.134	9.415e-07
3	10414	0.071	1.209e-06
4	7442	0.030	1.209e-06
5	6683	0.029	1.209e-06

Table 5: Summary of numerical models data for the longitudinal impactor orientation.

Since the present finite element models are made with a uniform mesh size it is possible to apply different failure parameters to account for the mesh sensitivity of the ductile failure model. In a real engineering structure, the mesh size is most likely varying along the parts of the structure and thus an automatic mesh size regularisation rule is needed. Several mesh regularisation rules have been proposed in the literature and are usually formulated as follows

$$A_f = A_h + (A_l - A_h).h\left(\frac{l_e}{t_e}\right) \tag{5}$$

where A_f is the failure parameter for a particular mesh size, A_h is the failure parameter for a very large element size and A_l is the failure parameter for small elements. The function $h\,(l_e/t_e)$ depends on the element size; it decreases with increasing the element length and is equal to one when l_e/t_e is equal to one. Several failure models designed for structural steels have been proposed in the literature [10] and are usually similar in nature to Barba's law [35]. Figure 19 shows the results of two approaches to handle mesh regularisation of failure parameters using the data collected on the plate material (section 4.4). The first is the RTCL regularisation scheme proposed by Törnqvist [36]:

$$\varepsilon_f = \varepsilon_n + (\varepsilon_l - \varepsilon_n).\frac{t_e}{l_e} \tag{6}$$

where ε_f is the failure strain for a given mesh size, ε_n is the strain at diffuse necking and ε_l is the local strain at failure identified using an element aspect ratio of one. By assuming that the failure strain is the equivalent plastic strain, it is possible to determine the fracture parameter W_C using the isotropic hardening rule. In the second approach, denoted exponential decay, the fracture parameter

W_C is defined by

$$W_C = W_C^h + (W_C^l - W_C^h).e^{-c.\left(\frac{l_e}{t_e}-1\right)} \quad (7)$$

where W_C is the Cockcroft-Latham parameter for a given mesh size, W_C^h is the fracture parameter for large shell elements, W_C^l is the fracture parameter for an element with aspect ratio equal to one, and c is a model parameter. This model requires an optimisation of the parameters W_C^h and c in contrast to the regularisation proposed Törnqvist [36]. This optimisation is readily performed provided DIC measurements are available from the tensile tests.

The resulting evolution of the fracture parameter W_C as function of the mesh size is shown in Figure 19. The exponential decay funcion is able to reproduce rather accurately the evolution of the fracture parameter with element size and predicts a saturation around 40 MPa. The RTCL regularisation function is giving a conservative estimate of the failure parameter with a saturation at around 30 MPa.The parameters obtained for the plate and stiffener materials using the exponential decay function are summarised in Table 6.

Material	W_C^l (MPa)	W_C^h (MPa)	c (-)
Plate	64.4	39.9	0.62
Stiffener	64.3	30.9	0.33

Table 6: Parameters of the exponential decay function for the plate and stiffener materials.

Conclusions

The behaviour and failure of stiffened panels of aluminium alloy AA6082-T6 subjected to quasi-static and low-velocity impact loading was investigated experimentally and numerically. The experimental study showed that the quasi-static and dynamic tests gave similar results in terms of global behaviour and failure modes. This finding was attributed to the low rate sensitivity of the AA6082-T6 alloy and the large mass of the impactor compared with the mass of the stiffened panel. Failure in the stiffened panel was initiated by a ductile fracture process, while propagation seemed to be dominated by slant (shear) fracture. The proposed material model gave satisfactory results for fine shell element meshes with characteristic size of the order of the plate thickness. The mesh dependence of the failure predictions was reduced by the suggested identification approach for the fracture parameter using digital image correlation, as long as the deformation mode of the stiffened panel was aptly described.

Acknowledgements

The authors would like to acknowledge the Centre for Advanced Structural Analysis for the financial support, SAPA and Hydro for supplying the welded aluminium panels. The authors would like to acknowledge the support from MSc Sindre Solvernes for his support during the design of the test rig.

References

[1] W. Miller, L. Zhuang, J. Bottema, a.J Wittebrood, P. De Smet, a. Haszler, and a. Vieregge, "Recent development in aluminium alloys for the automotive industry," *Materials Science and Engineering: A*, vol. 280, no. 1, pp. 37–49, 2000.

[2] P. Rigo, R. Sarghiuta, S. Estefen, E. Lehmann, S. C. Otelea, I. Pasqualino, B. C. Simonsen, Z. Wan, and T. Yao, "Sensitivity analysis on ultimate strength of aluminium stiffened panels," *Marine Structures*, vol. 16, no. 6, pp. 437–468, 2003.

[3] A. Aalberg, M. Langseth, and P. Larsen, "Stiffened aluminium panels subjected to axial compression," *Thin-Walled Structures*, vol. 39, no. 10, pp. 861–885, 2001.

[4] R. M. F. Paulo, F. Teixeira-Dias, and R. A. F. Valente, "Numerical simulation of aluminium stiffened panels subjected to axial compression: Sensitivity analyses to initial geometrical imperfections and material properties," *Thin-Walled Structures*, vol. 62, pp. 65–74, 2013.

[5] H. S. Alsos and J. Amdahl, "On the resistance to penetration of stiffened plates, Part I - Experiments," *International Journal of Impact Engineering*, vol. 36, no. 6, pp. 799–807, 2009.

[6] E. Lehmann and J. Peschmann, "Energy absorption by the steel structure of ships in the event of collisions," *Marine Structures*, vol. 15, pp. 429–441, 2002.

[7] B. Liu, R. Villavicencio, and C. Guedes Soares, "Simplified analytical method to evaluate tanker side panels during minor collision incidents," *International Journal of Impact Engineering*, vol. 78, pp. 20–33, 2015.

[8] H. S. Alsos, J. Amdahl, and O. S. Hopperstad, "On the resistance to penetration of stiffened plates, Part II: Numerical analysis," *International Journal of Impact Engineering*, vol. 36, no. 7, pp. 875–887, 2009.

[9] M. Storheim, H. S. Alsos, O. S. Hopperstad, and J. Amdahl, "A damage-based failure model for coarsely meshed shell structures," *International Journal of Impact Engineering*, vol. 83, pp. 59–75, 2015.

[10] M. A. G. Calle and M. Alves, "A review-analysis on material failure modeling in ship collision," *Ocean Engineering*, vol. 106, pp. 20–38, 2015.

[11] M. Fourmeau, T. Børvik, A. Benallal, and O. S. Hopperstad, "Anisotropic failure modes of high-strength aluminium alloy under various stress states," *International Journal of Plasticity*, vol. 48, pp. 34–53, 2013.

[12] T. Wang, O. S. Hopperstad, O. G. Lademo, and P. K. Larsen, "Finite element analysis of welded beam-to-column joints in aluminium alloy EN AW 6082 T6," *Finite Elements in Analysis and Design*, vol. 44, no. 1-2, pp. 1–16, 2007.

[13] J. Adamowski and M. Szkodo, "Friction Stir Welds (FSW) of aluminium alloy AW6082-

T6," *Journal of Achievements in Materials and Manufacturing Engineering*, vol. 20, no. 1-2, pp. 403–406, 2007.

[14] F. Barlat, J. C. Brem, J. W. Yoon, K. Chung, R. E. Dick, D. J. Lege, F. Pourboghrat, S. H. Choi, and E. Chu, "Plane stress yield function for aluminum alloy sheets - Part 1: Theory," *International Journal of Plasticity*, vol. 19, no. 9, pp. 1297–1319, 2003.

[15] F. Grytten, B. Holmedal, O. S. Hopperstad, and T. B??rvik, "Evaluation of identification methods for YLD2004-18p," *International Journal of Plasticity*, vol. 24, no. 12, pp. 2248–2277, 2008.

[16] K. Zhang, B. Holmedal, O. S. Hopperstad, S. Dumoulin, J. Gawad, A. Van Bael, and P. Van Houtte, "Multi-level modelling of mechanical anisotropy of commercial pure aluminium plate: Crystal plasticity models, advanced yield functions and parameter identification," *International Journal of Plasticity*, vol. 66, pp. 3–30, 2015.

[17] M. Khadyko, S. Dumoulin, T. Børvik, and O. S. Hopperstad, "An experimental-numerical method to determine the work-hardening of anisotropic ductile materials at large strains," *International Journal of Mechanical Sciences*, vol. 88, pp. 25–36, 2014.

[18] Y. Bai and T. Wierzbicki, "Application of extended Mohr-Coulomb criterion to ductile fracture," *International Journal of Fracture*, vol. 161, no. 1, pp. 1–20, 2010.

[19] M. Luo, M. Dunand, and D. Mohr, "Experiments and modeling of anisotropic aluminum extrusions under multi-axial loading - Part II: Ductile fracture," *International Journal of Plasticity*, vol. 32, no. 33, pp. 36–58, 2012.

[20] G. Gruben, O. S. Hopperstad, and T. Borvik, "Evaluation of uncoupled ductile fracture criteria for the dual-phase steel Docol 600DL," *International Journal of Mechanical Sciences*, vol. 62, no. 1, pp. 133–146, 2012.

[21] E. Fagerholt, *Field measurements in mechanical testing using close-range photogrammetry and digital image analysis*. PhD thesis, Norwegian University of Science and Technology, 2011.

[22] G. Gruben, S. Sølvernes, T. Berstad, D. Morin, O. S. Hopperstad, and M. Langseth, "Low-velocity impact behaviour and failure of stiffened steel plates," *Marine Structures*, accepted

for publication.

[23] A. G. Hanssen, T. Auestad, T. Tryland, and M. Langseth, "The kicking machine: A device for impact testing of structural components," *International Journal of Crashworthiness*, vol. 8, no. 4, pp. 385–392, 2003.

[24] Y. Chen, A. H. Clausen, O. S. Hopperstad, and M. Langseth, "Stress-strain behaviour of aluminium alloys at a wide range of strain rates," *International Journal of Solids and Structures*, vol. 46, no. 21, pp. 3825–3835, 2009.

[25] A. Saai, S. Dumoulin, O. S. Hopperstad, and O. G. Lademo, "Simulation of yield surfaces for aluminium sheets with rolling and recrystallization textures," *Computational Materials Science*, vol. 67, pp. 424–433, 2013.

[26] A. V. Hershey, "The plasticity of an isotropic aggregate of anisotropic face centred cubic crystals," *Journal of Applied mechanics*, vol. 21, pp. 241–249, 1954.

[27] W. F. Hosford, "A generalized isotropic yield criterion," *Journal of Applied mechanics*, vol. 39, no. 2, pp. 607–609, 1972.

[28] M. Cockcroft and D. Latham, "Ductility and Workability of Metals," *Journal of the institute of metals*, vol. 96, pp. 33–39, 1968.

[29] Dassault Systèmes Simulia, "Abaqus 6.14 / Analysis User's Guide," 2014.

[30] M. Ortiz and J. C. Simo, "An analysis of a new class of integration algorithms for elasoplastic constitutive relations," *International Journal for Numerical Methods in Engineering*, vol. 23, no. January 1985, pp. 353–366, 1986.

[31] T. Belytschko, W. K. Liu, and B. Moran, *Nonlinear finite elements for continua and structures*. Wiley, 2000.

[32] G. Gruben, D. Morin, M. Langseth, and O. Hopperstad, "Strain localization and ductile fracture in advanced high-strength steel sheets," *European Journal of Mechanics - A/Solids*, vol. 61, pp. 315–329, jan 2017.

[33] P. Hogström, J. W. Ringsberg, and E. Johnson, "An experimental and numerical study of the effects of length scale and strain state on the necking and fracture behaviours in sheet metals," *International Journal of Impact Engineering*, vol. 36, no. 10-11, pp. 1194–1203,

2009.

[34] C. Dørum, O. G. Lademo, O. R. Myhr, T. Berstad, and O. S. Hopperstad, “Finite element analysis of plastic failure in heat-affected zone of welded aluminium connections,” *Computers and Structures*, vol. 88, no. 9-10, pp. 519–528, 2010.

[35] M. Barba, “No Title,” *Mémoires de la société des ingénieurs civils*, pp. 682–714, 1880.

[36] R. Törnqvist, *Design of crashworthy ship structures*. PhD thesis, Technical University of Denmark, 2003.

List of Figures

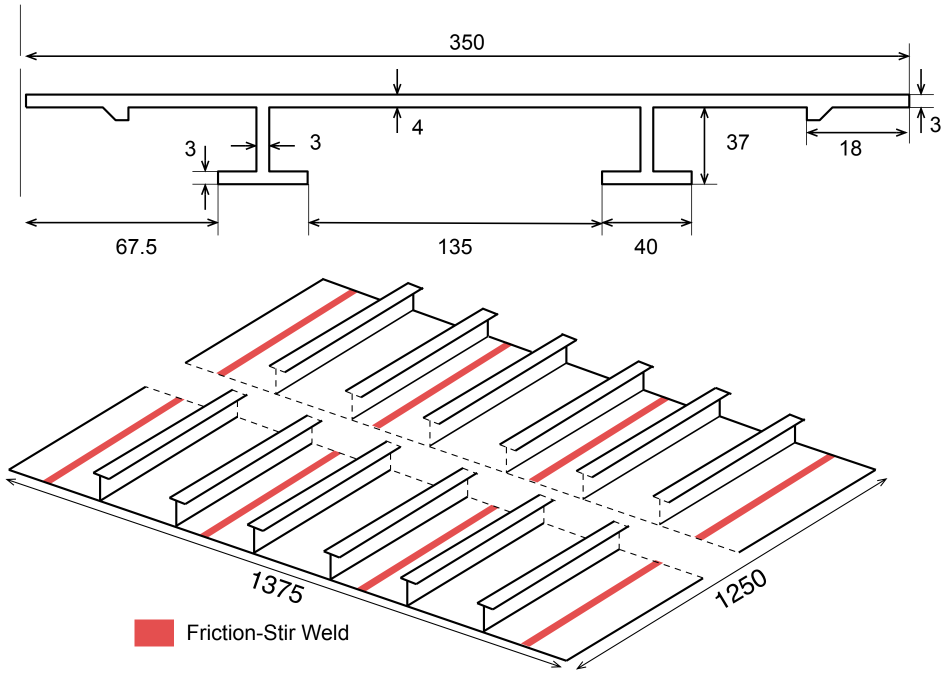

Figure 1: Illustration of the extruded profile and the assembled panels.

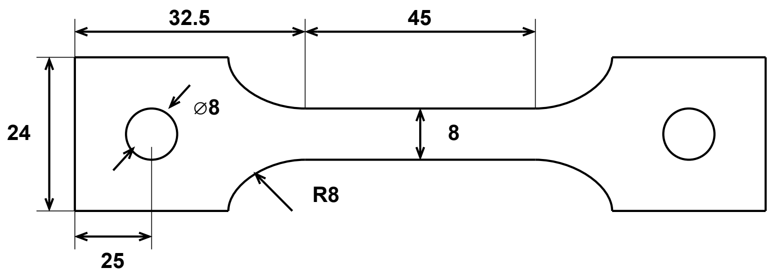

a) Plate and stiffener material

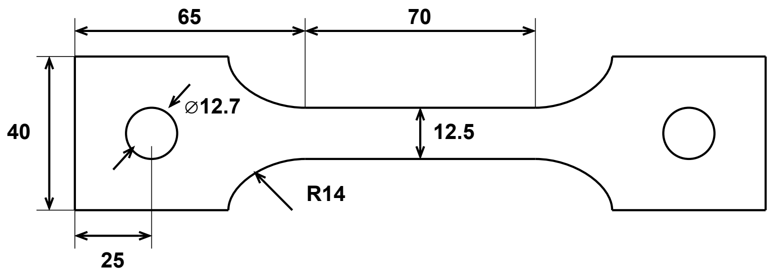

b) Specimen crossing the HAZ

Figure 2: Geometry of the tensile specimens.

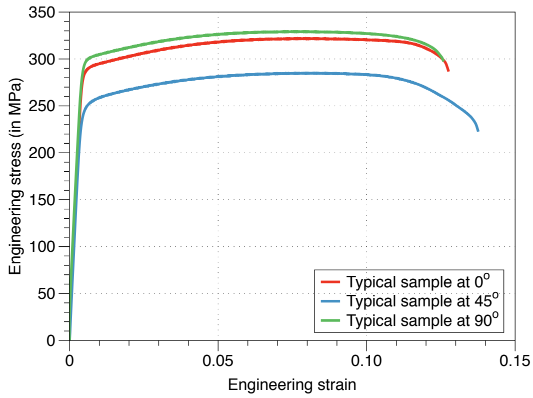

a) Plastic anisotropy of plate material

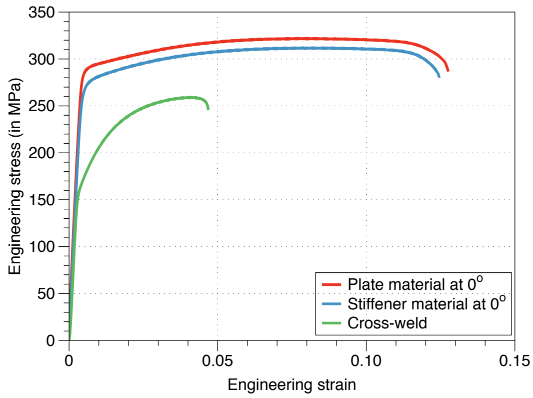

b) Plate, stiffener and HAZ materials

Figure 3: Stress-strain curves of AA6082 in temper T6.

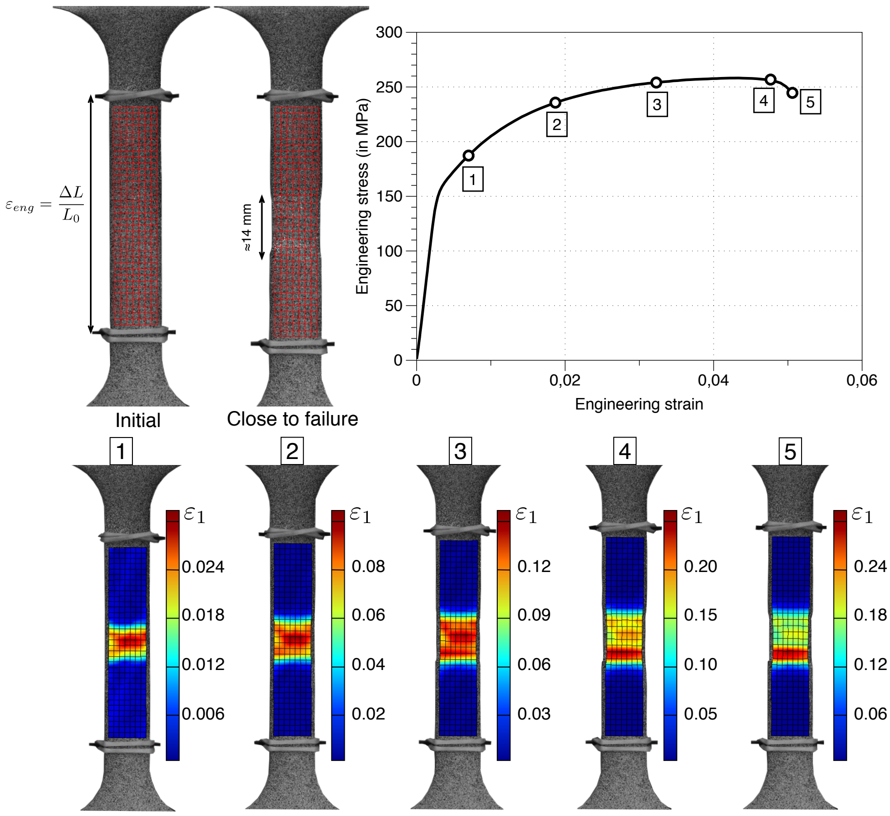

Figure 4: Heterogeneous strain field in the cross-weld tensile tests.

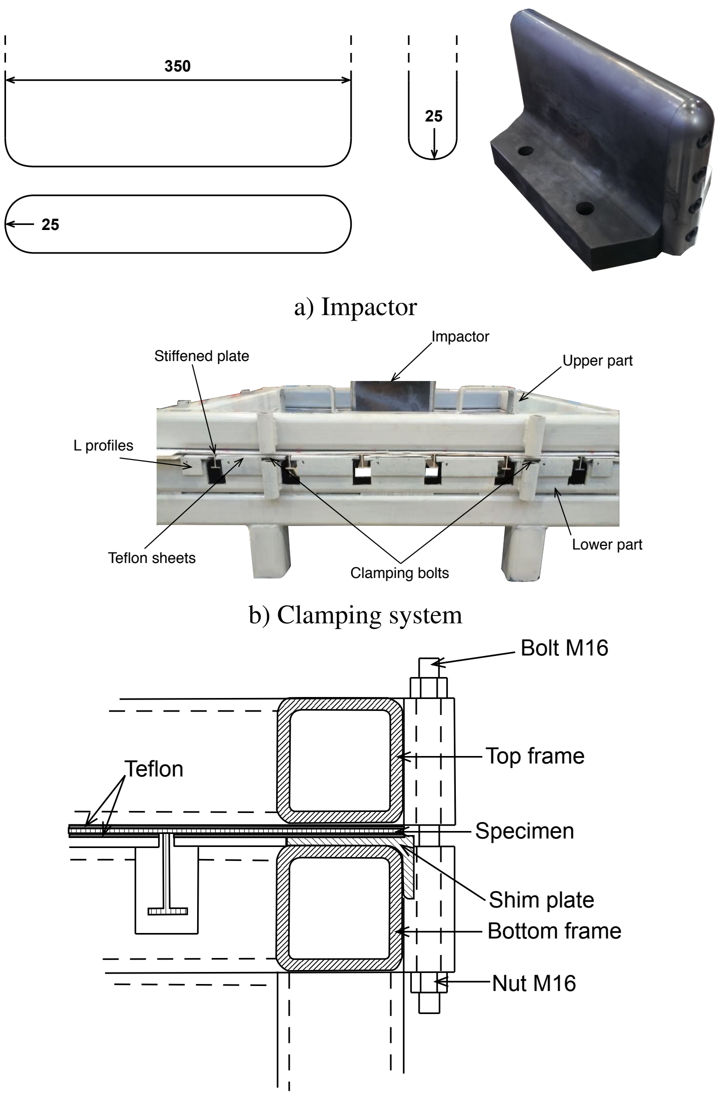

a) Impactor

b) Clamping system

c) Close-up view

Figure 5: Shape of the impactor and clamping system for stiffened panel tests.

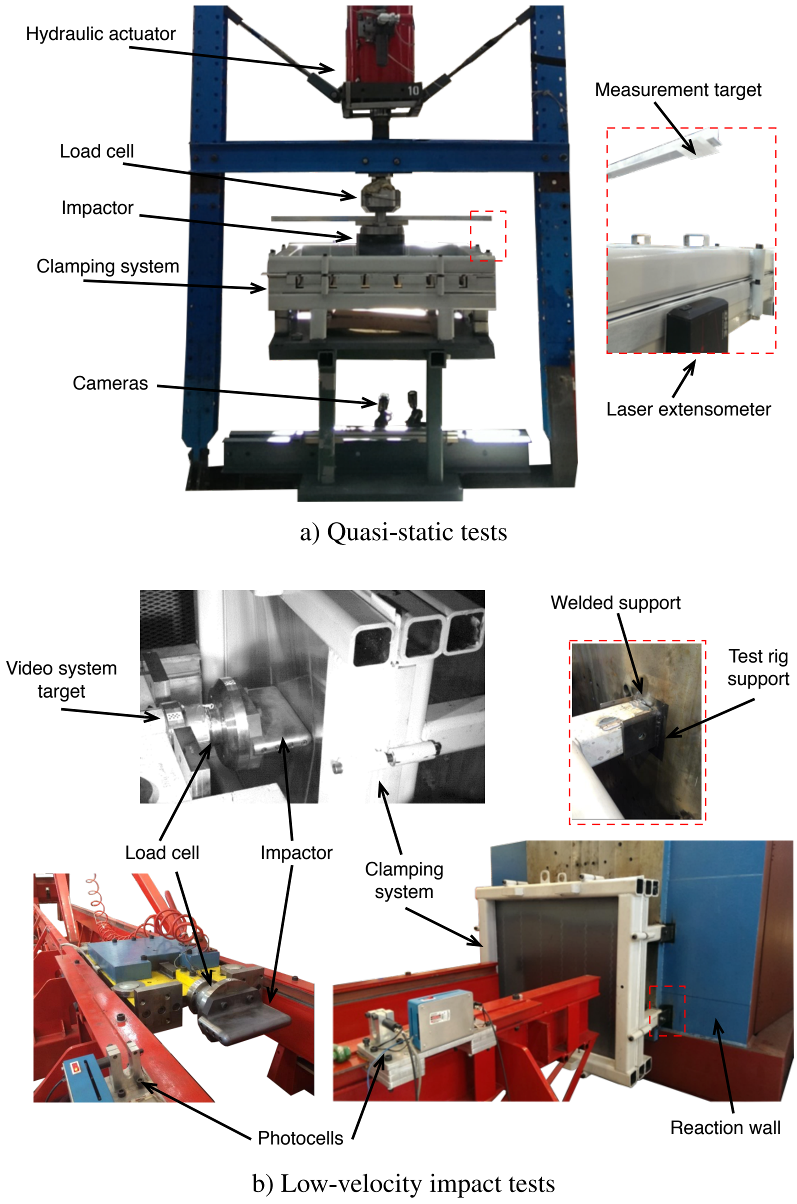

Figure 6: Setups for component tests.

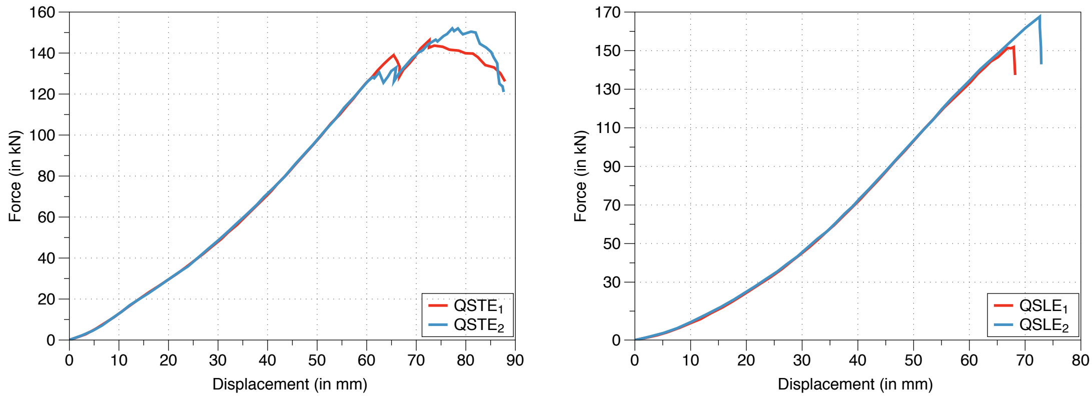

a) Transverse impactor orientation

b) Longitudinal impactor orientation

Figure 7: Force-displacement curves from the quasi-static tests.

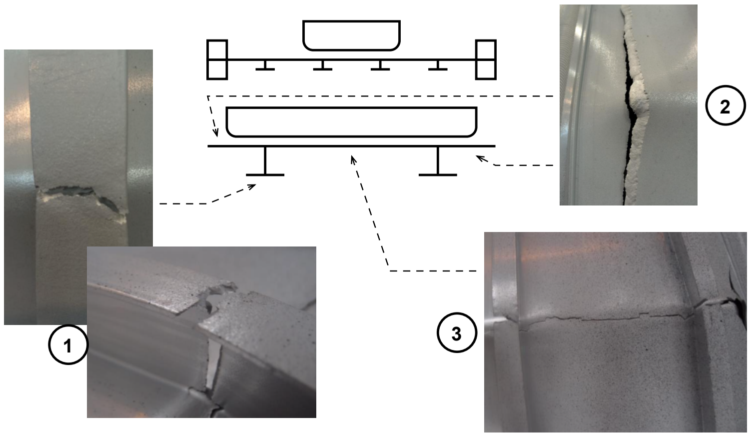

a) Transverse impactor orientation

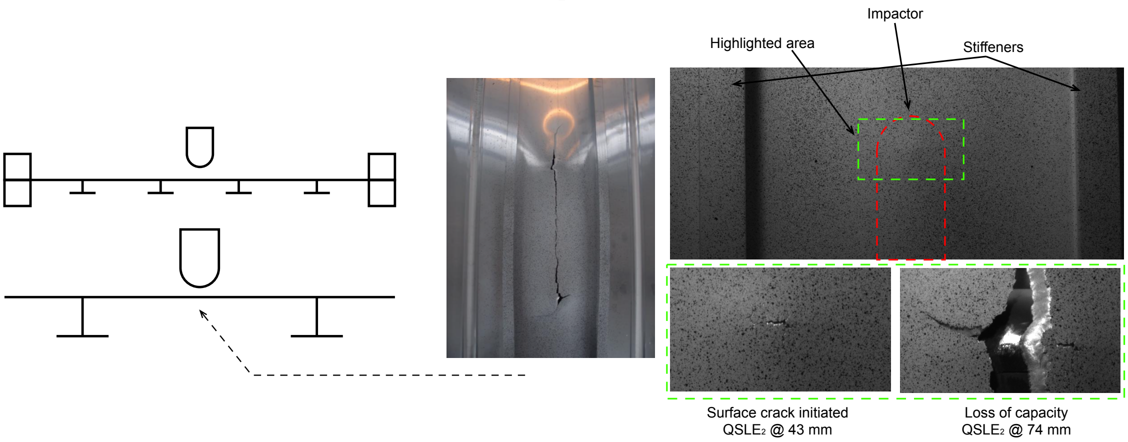

b) Longitudinal impactor orientation

Figure 8: Observed fracture in the quasi-static tests.

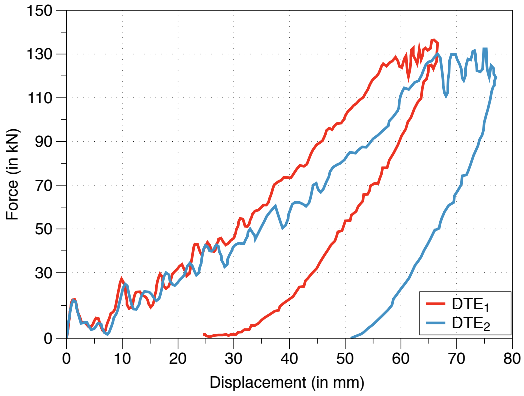

a) Transverse impactor orientation

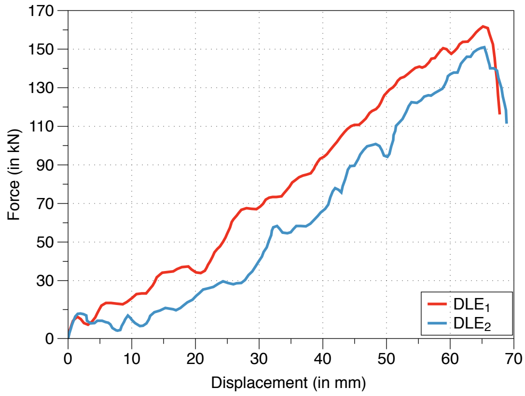

b) Longitudinal impactor orientation

Figure 9: Force-displacement curves from the low-velocity impact tests.

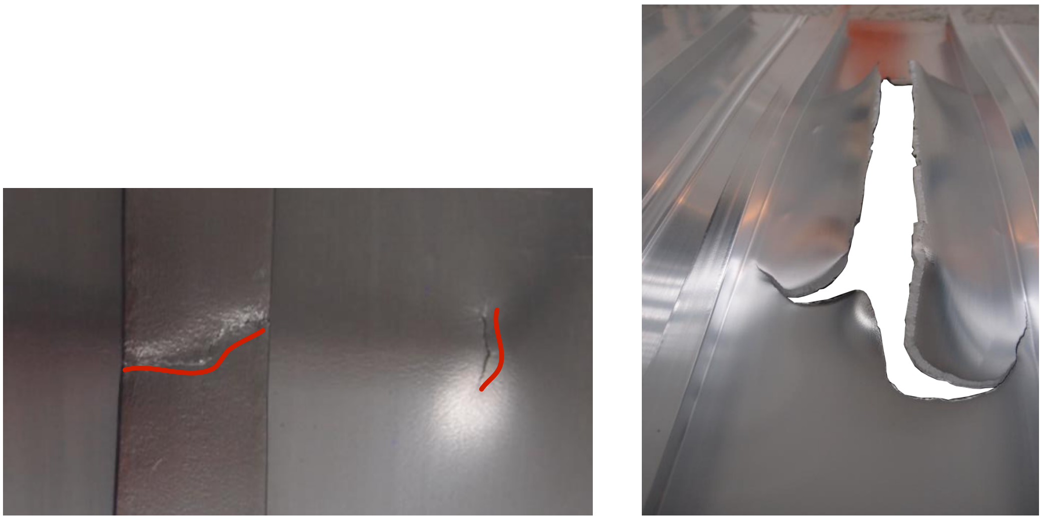

a) Transverse impactor orientation
b) Longitudinal impactor orientation

Figure 10: Observed fracture in the low-velocity impact tests.

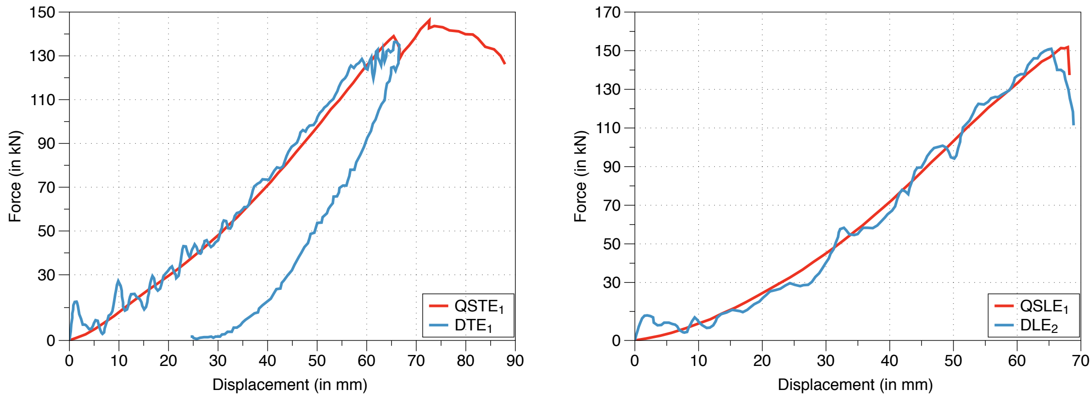

a) Transverse impactor orientation

b) Longitudinal impactor orientation

Figure 11: Comparison between quasi-static and low-velocity impact tests.

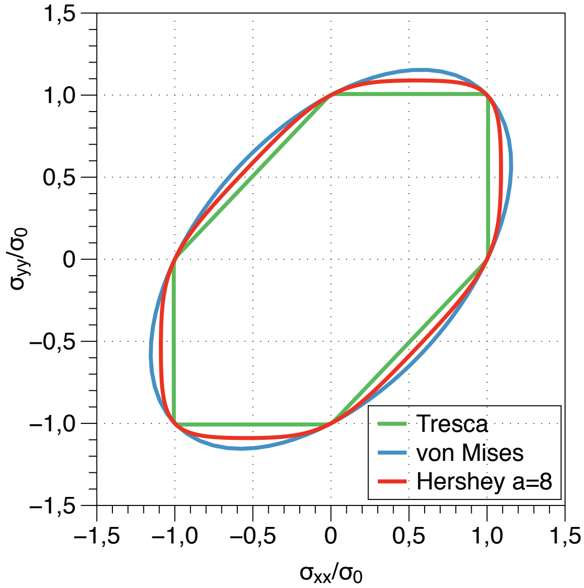

Figure 12: Hershey-Hosford yield surface under plane stress.

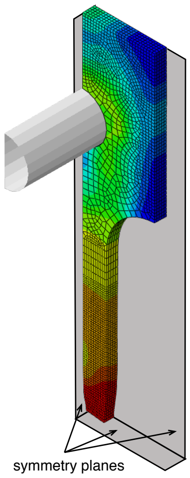

a) Finite element model of tensile test

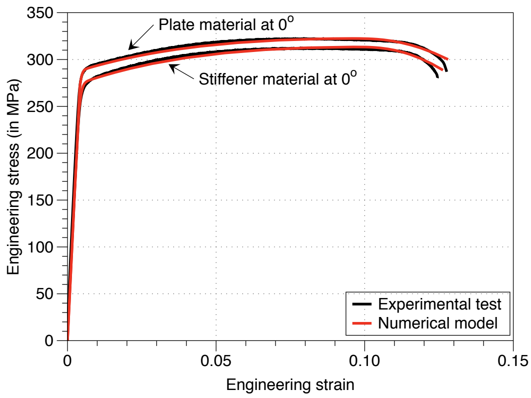

b) Results from the reverse engineering procedure

Figure 13: Identification of the work-hardening parameters.

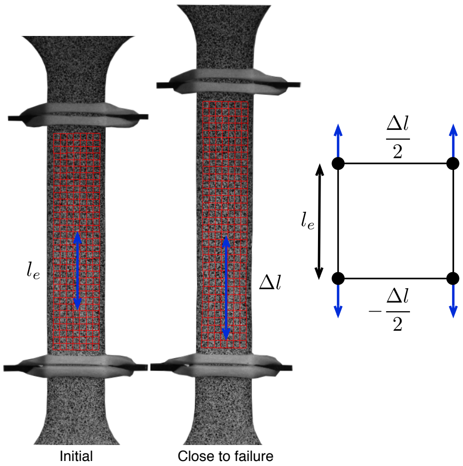

a) Identification method

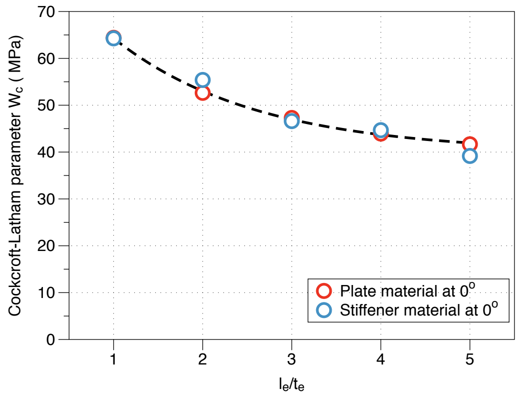

b) Results

Figure 14: Identification of the failure parameter.

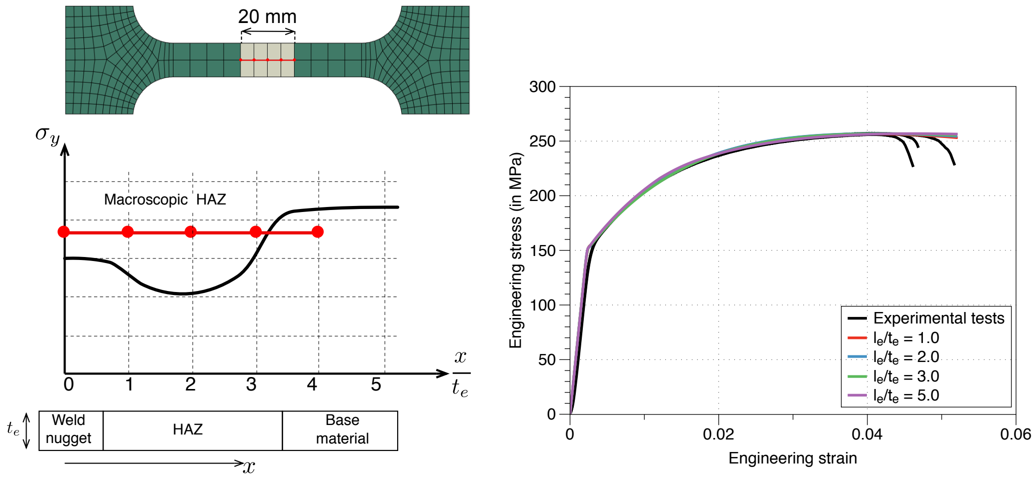

a) Identification method

b) Results

Figure 15: Identification of the macroscopic HAZ parameters.

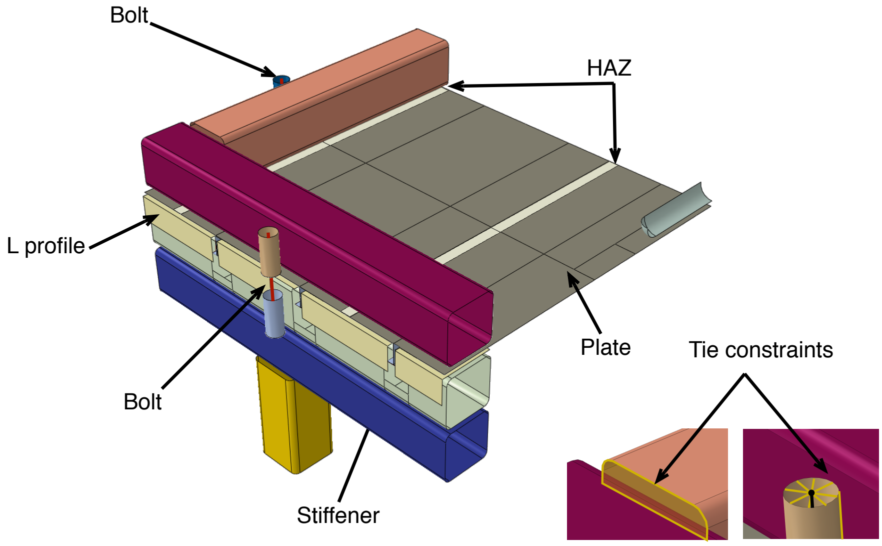

Figure 16: Numerical setup for the component tests.

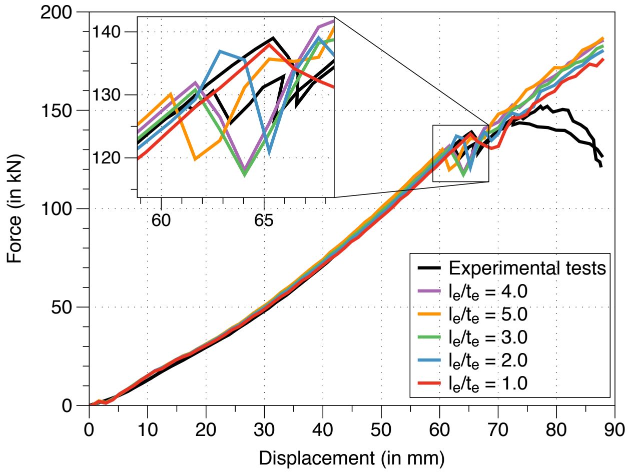

a) Force-displacement curves

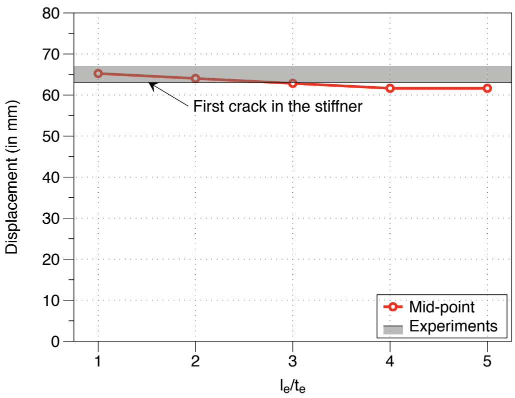

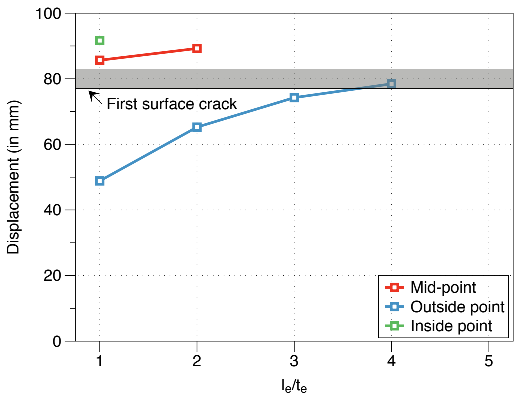

b) Failure in the stiffener material

c) Failure in the plate material

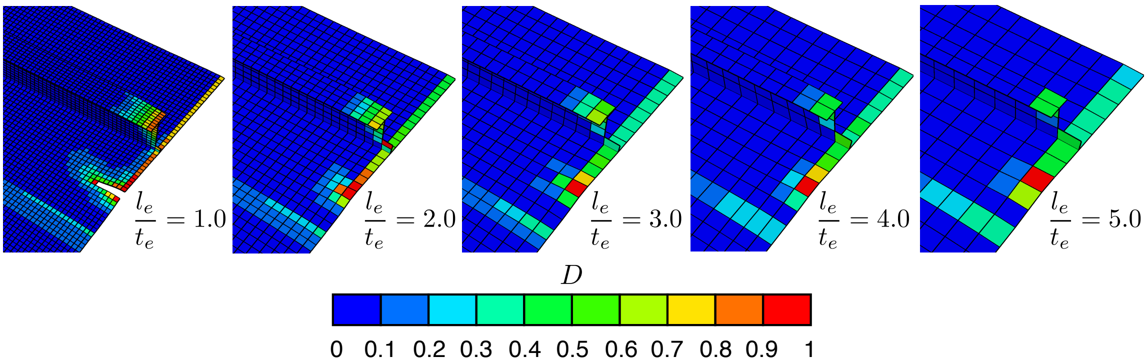

d) Damage fields on deformed specimens

Figure 17: Results for the transverse impactor orientation.

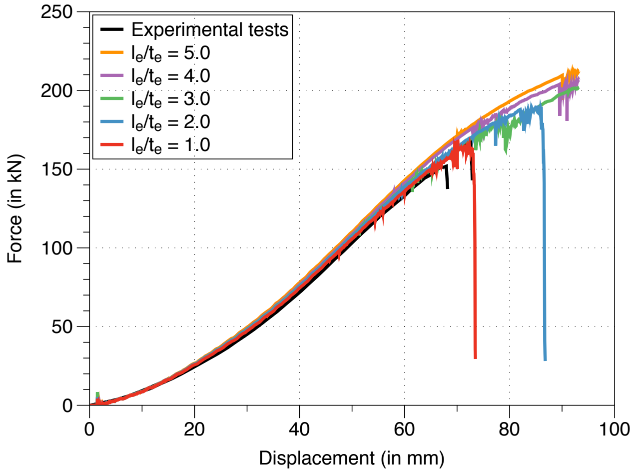

a) Force-displacement curves

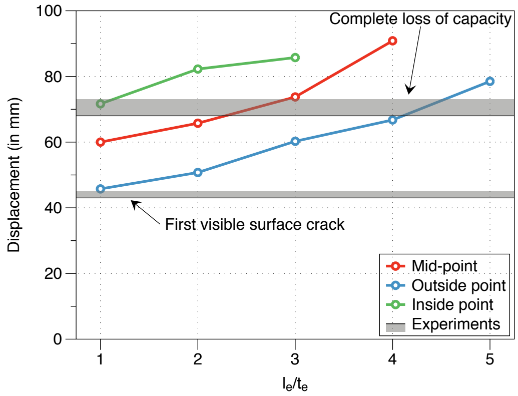

b) Failure in the plate material

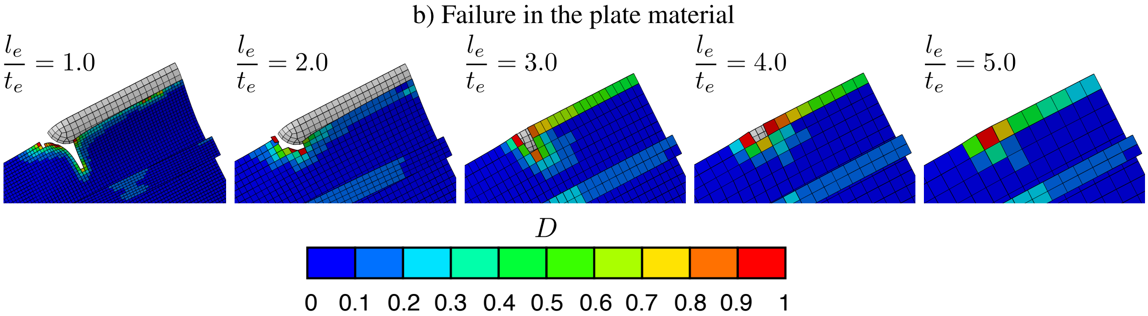

c) Damage fields on deformed specimens

Figure 18: Results for the longitudinal impactor orientation.

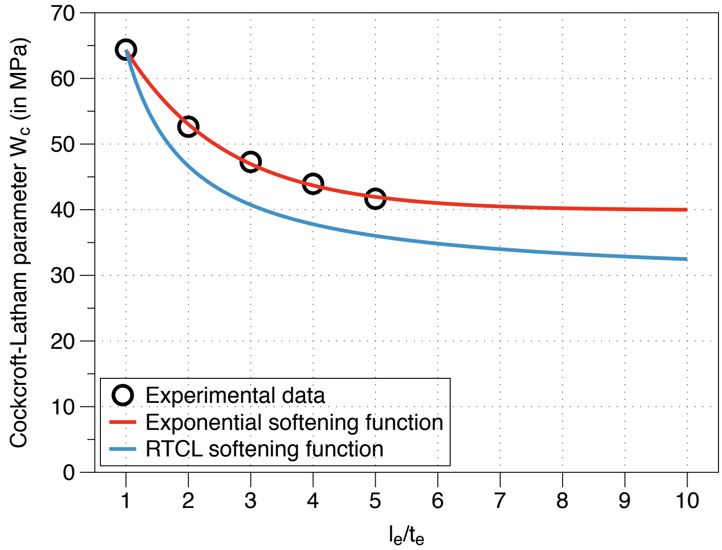

Figure 19: Illustration of mesh size regularization models.